



LAWRENCE
LIVERMORE
NATIONAL
LABORATORY

Deuterium-tritium fuel layer formation for the National Ignition Facility

B. J. Kozioziemski, E. R. Mapoles, J. D. Sater, A.
A. Chernov, J. D. Moody, J. B. Lugten, M. A.
Johnson

April 21, 2010

Fusion Science and Technology

Disclaimer

This document was prepared as an account of work sponsored by an agency of the United States government. Neither the United States government nor Lawrence Livermore National Security, LLC, nor any of their employees makes any warranty, expressed or implied, or assumes any legal liability or responsibility for the accuracy, completeness, or usefulness of any information, apparatus, product, or process disclosed, or represents that its use would not infringe privately owned rights. Reference herein to any specific commercial product, process, or service by trade name, trademark, manufacturer, or otherwise does not necessarily constitute or imply its endorsement, recommendation, or favoring by the United States government or Lawrence Livermore National Security, LLC. The views and opinions of authors expressed herein do not necessarily state or reflect those of the United States government or Lawrence Livermore National Security, LLC, and shall not be used for advertising or product endorsement purposes.

Deuterium-tritium fuel layer formation for the National Ignition Facility

B. J. Kozioziemski, E. R. Mapoles, J. D. Sater, A. A. Chernov, J. D. Moody, J. B. Lugten, and M. A. Johnson
Lawrence Livermore National Laboratory, Livermore CA 94551

(Dated: April 19, 2010)

Inertial confinement fusion requires very smooth and uniform solid deuterium-tritium (D-T) fuel layers. The National Ignition Facility (NIF) point-design calls for the 65-75 μm thick D-T fuel layer inside of a 2 mm diameter spherical ablator to be 1.5 K below the D-T melting temperature (T_m) of 19.79 K. We find that the layer quality depends on the initial crystal seeding, with the best layers grown from a single seed. The low modes of the layer are controlled by thermal shimming of the hohlraum and meet the NIF requirement with beryllium shells and nearly meet the requirement with plastic shells. The remaining roughness is localized in grain-boundary grooves and is minimized when grown from a single crystal. Once formed, the layers need to be cooled to $T_m - 1.5$ K. We have studied dependence of the roughness on the cooling rate and found that cooling at rates of 0.03 K/s - 0.5 K/s is able to preserve the layer structure for a few seconds after reaching the desired temperature. The fuel layer remains in good contact with the shell during this rapid cooling. Thus, rapid-cooling of the layers is able to satisfy the NIF ignition requirements.

PACS numbers:

INTRODUCTION

The experiments to test inertial confinement fusion are being undertaken at several facilities, including the National Ignition Facility (NIF). Successful ignition requires that the targets meet many stringent specifications, such as positioning, fuel and ablator areal density uniformity, thickness, and composition[1]. One of the more challenging aspects is the solid deuterium-tritium (D-T) fuel layer. Since the D-T solidifies at low temperature, must be in a spherical geometry, and has a finite lifetime due to the generation of helium-3, mechanical methods for preparation of the surface cannot be used. Fortunately, the D-T layers will naturally smooth in a process termed beta-layering[2, 3]. The heat generated by the radioactive decay causes the D-T surface to tend toward a smooth surface to minimize the volumetric energy. However, crystal facets, grain boundaries, and other surface features limit the smoothing. Several groups continue to explore methods to form the D-T layers to minimize the roughness[4–8]. Most studies of D-T and D_2 layer formation are done by slowly solidifying from the liquid. Another approach that has been studied is to flash-freeze the solid directly from the vapor phase[9]. The use of infrared (IR) heating to produce smooth HD, D_2 , and D-T layers has also been demonstrated[10, 11]. Fuel layers for the initial NIF ignition experiments will be formed by solidifying from the liquid, without the use of IR heating because the baseline ablator choices are plastic, which absorbs IR too strongly compared to D-T[12], and beryllium, which reflects IR. This approach is the focus of this paper.

The NIF ignition point design is described in detail[1], and only those details relevant to the D-T fuel layer are reviewed here. The NIF ignition point design requires a 65-75 μm thick solid D-T layer inside of a 2 mm diameter spherical plastic or beryllium ablator. The central region of the spherical capsule is filled with D-T vapor at the solid's saturated vapor density for a given temperature. The fusion yield is predicted to

be improved by reducing the central vapor density from the value at the triple-point temperature (T_{TP}) of 0.6 mg/cc to 0.3 mg/cc, which corresponds to reducing the solid temperature from 19.79 K to 18.3 K.

The relevant NIF ignition requirement for the D-T surface roughness is given in three parts. The first is the shape, expressed as the first 6 modes in the power spectral density (PSD) obtained from a Fourier analysis of the radius as a function of the angular position. These are modes which are most strongly coupled to the thermal environment and can be controlled by adjusting the four heaters on the hohlraum[13, 14], termed thermal shimming. The second requirement is the high modes of the PSD, modes 7-128. This is controlled by the surface properties and beta-layering of the D-T, and is largely determined by the initial formation of the fuel layer. The third requirement is a local-defect specification, termed the “K” specification. K assumes that the local defects are primarily grain-boundary grooves on the D-T surface. This requirement is similar to the high-mode roughness requirement except that the high-mode roughness assumes that the roughness in the power spectrum is randomly phased, or uniformly distributed over the entire surface. Instead, if the roughness is localized, as in grain-boundary grooves, then that groove's contribution to the hot-spot degradation is much higher than expressed as an RMS.

The requirement that $A < 200 \mu\text{m}^2$ is more restrictive than the high-mode PSD requirement. Figure 1 shows the PSD calculated for several grooves compared to the D-T fuel layer PSD requirement. We see that the groove could easily meet the PSD requirement while still exceeding the $A < 200 \mu\text{m}^2$.

The second requirement for isolated defects is that the weighted sum, known as the K specification, is less than 0.7 μm , where

$$K = \sqrt{\frac{\sum_i A_i^2 L_i}{V}}, \quad (1)$$

where V is the volume of the fuel layer, used as a normalization, A_i is the area of groove i and L_i is its length. This re-

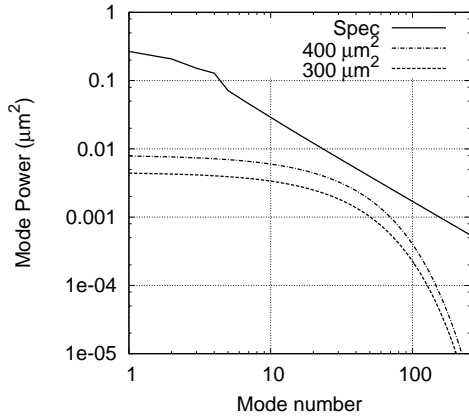


FIG. 1: Calculated power spectrum for $300 \mu\text{m}^2$ and $400 \mu\text{m}^2$ cross-sectional area grooves compared to the NIF specification for the surface roughness. Note that while both grooves would easily pass the PSD requirement, they both exceed the local defect specification of $200 \mu\text{m}^2$.

quirement turns out to be easy to meet given that all the groove areas are less than $200 \mu\text{m}^2$. With $A = 200 \mu\text{m}^2$, $V = 7.6 \times 10^8 \mu\text{m}^3$, then $L = 9370 \mu\text{m}$, or about 1.6 times around the D-T surface. With $A = 100 \mu\text{m}^2$, the total length can be just over 6 times around the surface and meet the K requirement.

This paper provides an overview of the layer formation process, including the seeding, characterization of surfaces, and rapid-cooling results. We show that the best layers are single crystals and that the rapid-cooling approach preserves the D-T surface long enough for ignition experiments. In contrast, the slow-cooling method is unable to produce layers without local defects. The paper is organized as follows. The experimental configuration and characterization methods will be outlined first. The initial layer formation will be discussed, as well as the slow and rapid cooling protocols. The resulting change in roughness during cooling, defect profiles, and adhesion between the D-T and ablator will be presented in the discussion section.

METHOD

Experiments were conducted using NIF geometry capsules and hohlraum assemblies. The capsules are nominally 2 mm inner diameter with wall thickness of 40 - 165 μm , depending on the experiment. A fill-hole is laser drilled through the capsule wall and a 5-10 μm fill-tube is epoxied into the hole[15]. The capsule is evacuated and D-T admitted to the capsule through the fill-tube. The hohlraum is thermally and mechanically connected to the cold-stage of a cryostat. The hohlraum is usually sealed with windows, with 1-300 torr of ^4He gas in the hohlraum to conductively cool the capsule. In some cases the hohlraum leaks and ^4He is also present in the space around the hohlraum. Four thermometers and heaters are attached to the hohlraum. D-T is supplied to the shell via

the fill-tube.

The layers were characterized by both optical shadowgraphy[16] and phase-contrast enhanced x-ray imaging[17, 18]. Both methods characterize the PSD roughness by detecting an edge in the image which corresponds to the D-T solid-vapor interface and Fourier transforming the resulting radius as a function of angle. The x-ray imaging can provide more quantitative measurement the D-T surface roughness than the optical shadowgraphy, however it requires several minutes to acquire enough x-ray photons to produce an image with suitable signal-to-noise for analysis. In contrast, the shadowgraph takes less than a second to obtain an image, but only works with plastic shells and is subject to large refraction. The optical imaging also provides more contrast from small features than the x-ray imaging, making it useful in detecting small defects. Thus the shadowgraph is used during rapid cooling to observe the layer evolution. Additional details of the shadowgraphy and x-ray imaging are described elsewhere[16–18].

One deviation from past shadowgraphy characterizations is that we now focus the microscope on the D-T surface rather than at the center-plane of the capsule. This is because the bright-band due to the total-internal reflection historically used to characterize the D-T layer is of limited use for local defects. The localized defects typically result in severe distortion of the bright-band and cannot be used to determine the extent of the defect. Instead, focusing on the D-T surface enables us to observe the initial seeding and layer growth, development of grain-boundary grooves, and the correlation of the two. X-ray imaging is used to measure the fuel layer PSD and is more resilient to distortions from grain-boundary grooves, though large grooves will impact the measurement.

Both the x-ray imaging and optical microscopy are limited in their characterization of localized defects. A visible light interferometer was added to measure the profiles of the local defects. We used a phase shifting diffraction interferometer (PSDI) in transmission mode. The PSDI operation is as follows. The laser beam is split and injected into two fibers, one path having a variable phase delay. The light from one fiber, the object beam, passes through the cryostat and shell and is collected by a lens which refocuses the light to a spot on a mirror with a pinhole. The light from the second fiber, the reference beam, emerges from the pinhole as a nearly perfect spherical wave. Both beams travel from the mirror to a CCD where their interference pattern is recorded. A sequence of interferograms are recorded by the CCD with known steps in the phase of the delay line. The amplitude and phase of the object beam is then calculated and numerically propagated back to the plane of interest, in this case, the D-T surface, to obtain height variations at the optical plane. Our analysis uses 1.16 as the value of the D-T refractive index[19]. The height variations from the capsule are typically 1-2 orders of magnitude lower than that of the D-T layer, as verified by first imaging an empty shell. Furthermore, relative motion due to mechanical vibrations causes error in the interferogram analysis. Typical empty shell RMS roughness, which include both capsule

imperfections and vibration effects, were on the order of 10 nm. These variations are small compared to the 800 nm RMS specification for the D-T layer. A complete set of interferograms could be collected in 0.5 s, making this suitable for rapid cooling experiments.

The visible light images are useful in characterizing the initial seeding mechanism, the crystal orientation, and determining if it is a single crystal. The x-ray images provide low mode and high-mode RMS roughness measurements. The interferometer provides a detailed view of the local defects. Thus we can correlate the initial crystal seeding, based on the visible light images, with the roughness and groove information in the x-ray and PSDI.

LAYER SEEDING AND LAYER FORMATION

We have previously found that the D-T layers with the fewest defects are single crystal[20, 21]. This is because vapor-etched grain-boundary grooves form at the boundaries between different crystals. Therefore, it is necessary to start the layer formation from a single “seed” crystal. In previous experiments a single seed crystal was obtained by starting from solid D-T in the shell then slowly melting until only liquid remained in the capsule, but keeping the temperature within 5 mK of T_{TP} . Then when the shell is slowly re-cooled at rates of 0.25 mK/min - 2 mK/min a single crystal often emerged from the 30-40 μm diameter fill-tube[20]. It was likely that solid remained in the fill-tube and geometrical selection of the regrowing crystal selected a single crystal with the fast-growing a-direction parallel to the fill-tube axis. The temperature of the capsule was lowered to 100-200 mK below T_{TP} at the above rates, allowing the solidification to proceed over several hours.

However, in more recent experiments with the NIF required 5-10 μm diameter fill-tubes, a new meta-stable behavior was observed[22]. This meta-stable solid emerges from the fill-tube, grows into the liquid and spontaneously recrystallized to the hcp solid, typical of the hydrogens solidified from the liquid. The recrystallization usually results in a polycrystalline solid with many grain boundaries and unacceptable roughness. In some shells, nearly every seed attempt resulted in the meta-stable solid appearing first. However, it was observed the meta-stable solid could be triggered to recrystallize with a temperature pulse. Thus, it was necessary to alter the seeding processes to obtain a seed which was a single hcp crystal in the shell.

The current seeding process is as follows. The required amount of liquid is condensed into the shell and then the shell is quickly cooled to solidify the liquid and prevent mass transfer through the fill-tube. Next, the shell is warmed and the solid slowly melted in the capsule. Liquid pools in the bottom of the shell and forms a meniscus as the solid melts. The height of the meniscus above the capsule is tracked and complete melting is noted as the temperature when the meniscus height stops increasing. At this point the temperature is re-

duced by 30 - 50 mK, usually resulting in the meta-stable emerging from the fill-tube. The temperature is cycled by $\approx \pm 20$ mK to trigger the conversion to the hcp solid while the meta-stable solid is still relatively small. This typically results in hcp solid with a small number of relatively large crystals. Next, the temperature is again raised toward T_{TP} , this time stopping ≈ 0.5 -1.5 μm before the maximum meniscus height is reached. This often results in a single crystal remaining in the shell that serves as the seed crystal for the layer. The solidification proceeds by slowly cooling the shell by ≈ 100 mK over 8 - 16 hours.

Local defects appear during the layer formation even when solidification begins from a single crystal. Two classes of defects are observed. The first are what appear to be low-angle grain-boundary grooves which run normal to the crystal growth front, or along lines of longitude. These are likely the result of stacking faults or similar defects in the crystal lattice during solidification. The second class of defects are what we term “arctic circles” because they appear near the pole of the crystal and often are nearly concentric about the pole. While the arctic circles are probably also low-angle grain boundaries, their formation mechanism is not completely understood. It is often observed that the liquid is completely solidified before the poles are filled in. Thus the solid migrates to the poles due to beta-layering and grows by solid-vapor-solid rather than the liquid-solid growth for most of the layer. One hypothesis is that fewer defects occur with the liquid-solid transformation than the solid-vapor-solid. A second hypothesis is that the capsule curvature results in a continuous change in direction of the growth front with respect to the c-axis of the crystal. The crystal growth is along the c-axis when the growth front is not too far from the equator, but growth increasingly becomes along an a-axis of the crystal as it nears the pole. These arctic poles, while short in length, can have cross sectional areas that can exceed the specification.

Gradient Growth

A possible advantage of layer formation in the hohlraum is the ability to alter the temperature profile during the seeding and layer formation. We have tested layering with a larger temperature gradient along the hohlraum axis but have not had success in reliable layer formation.

The first use of the thermal gradient was to attempt to force a small seed crystal at the top of the shell, opposite the liquid meniscus. The probability of obtaining a single seed crystal increases as the size of the seed crystal is reduced. The process was to start with solid D-T in the shell, apply a 0.1 - 1 K temperature difference across the hohlraum, with the top colder than the bottom, then slowly increase the average temperature of the capsule to melt the solid. The solid initially migrates to the top of the shell, due to the thermal gradient, with an increasing amount of liquid accumulating at the bottom of the shell as the average temperature is increased. Contrary to expectations, the solid at the top of the shell could

not be made arbitrarily small. The last portion of the solid to melt typically was near the mid-plane of the shell for modest temperature differences across the hohlraum, less than ≈ 0.5 K. In those cases when the solid does remain at the top of the shell, it will often melt very quickly at the end. This latter effect is likely due to the crystal shrinking and growing primarily horizontally near the top of the capsule while the temperature gradient is vertical. Similarly, attempting to spontaneously nucleate a crystal at the top of the shell while in the thermal gradient failed because once nucleation occurred (typically at the fill tube) the solid rapidly grows laterally and becomes polycrystalline.

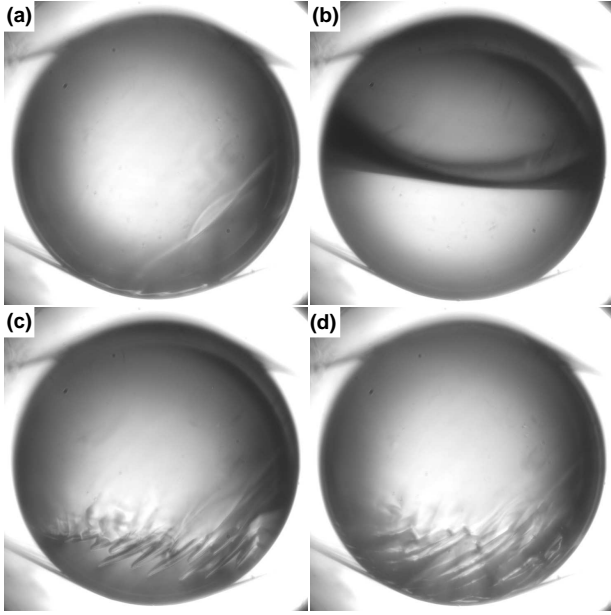


FIG. 2: Sequence showing attempt to use the thermal gradient to repair a defect in the D-T solid. The $40\ \mu\text{m}$ thick, 2 mm diameter CH shell is tented in a hohlraum with its axis vertical. Panel (a) shows the layer formed by slowly cooling from the liquid. The lower right corner has a visible defect. The temperature gradient has been applied along the hohlraum, with the top of the hohlraum 0.4 K colder than the bottom, in (b). The D-T responds by migrating to the top of the shell. The gradient is turned off over 4 hours, resulting in the redistribution of the D-T to the bottom of the shell. The image in (c) is taken 2 hours after (b), with a 0.2 K temperature difference across the hohlraum. A growth instability is apparent by the needle-like spikes in the growth front. (d) is taken with no gradient at the end of the recoiling and shows that the layer is significantly rougher than the starting condition in (a).

We tested the use of the thermal gradient to repair defects in the solid layer by evaporating and regrowing the defect region. In this case, the top temperature of the hohlraum was reduced and the bottom increased with the average temperature remaining constant. Thus, the solid D-T does not melt during this process. Figure 2 shows the result of one such attempt. The layer was formed by slow-cooling through from the liquid with no applied gradient and has a defect in the lower right section of the shell. The solid D-T is removed from the bot-

tom of the shell and driven to the top by making the top of the hohlraum 0.4 K colder than the bottom over approximately four hours. Figure 2(b) shows all of the solid D-T at the top of the shell and the bottom of the shell without any D-T. Next, the temperature gradient is removed over four hours, allowing the D-T to redistribute to the bottom of the shell. It was expected that the rate of advance of the D-T solid front could be controlled by the rate the gradient was turned off. However, Fig. 2(c), taken two hours into the redistribution, shows that the D-T growth front becomes unstable with needle-like growth as the front approaches the bottom of the shell. As mentioned above, the growth increasingly becomes parallel to, and hence unconstrained by, the temperature gradient. Figure 2(d) shows the final result after the gradient has been removed. The D-T layer has many large defects visible in the lower region of the shell and appears to be much rougher than the layer in (a). A similar result is obtained when the gradient is turned off over 10 hours. Thus attempting to redistribute the solid in the shell using a temperature gradient, perhaps to repair local defects that form during the initial growth, is unlikely to succeed.

Thermal shimming

In indirect drive ICF targets, the cylindrical shape of the hohlraum leads to isotherms that are not spherical at the solid D-T surface. Since the fuel layer is closer to the center of the hohlraum than the ends, the main effect of this is to introduce a mode 2 distortion into the shape of the fuel layer in which the fuel at the equator is thicker than the poles. In addition, in the hohlraums built for NIF ignition shots the heat removal from the two ends of the hohlraum is not perfectly symmetric. This results in a mode 1 distortion of the layer along the hohlraum axis, and a temperature difference is needed between the two ends to center the D-T layer in this direction.

Control of these two modes is performed by tailoring the temperature profile along the hohlraum axes with four heaters. Two of these heaters are used in control loops that control the temperatures of the ends of the hohlraum and allow a temperature gradient to be applied to adjust mode 1 to zero. The other two heaters, called shimming heaters, are wrapped around the body of the hohlraum. These shimming heaters are offset from the center of the hohlraum by approximately one capsule radius to provide access for imaging the target. When current is applied to these heaters, a trapezoidal temperature profile forms along the length of the hohlraum with the center being warmer than the ends. This counteracts the tendency of the fuel layer to be thicker at the equator and allows the mode 2 distortion to be adjusted to zero.

Figure 3 shows the measured mode 1 amplitude as the temperature difference at the arms supporting the hohlraum is adjusted. First we notice that the zero crossing of the mode 1 amplitude is not at zero temperature difference. This is likely due to a combination of differences in the thermometer calibrations and slight differences in the thermal resistance between the top and bottom paths from the hohlraum to the cryo-

stat cold tip. We find that the mode 1 sensitivity is $193 \mu\text{m/K}$ for this NIF scale plastic capsule. Therefore, controlling the temperature difference to within 1 mK will keep the mode 1 amplitude well below the NIF mode 1 requirement of $0.5 \mu\text{m}$. This resolution in temperature control is readily achieved with current instruments.

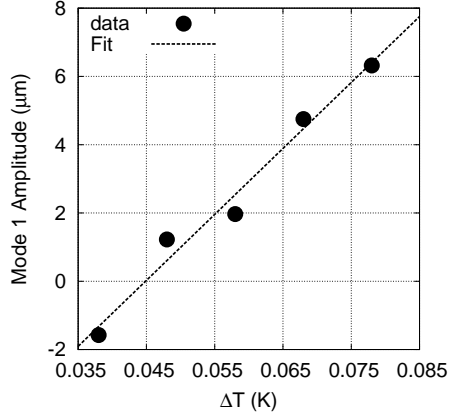


FIG. 3: Dependence of mode 1 amplitude of a $65 \mu\text{m}$ thick D-T layer on the measured temperature difference between the two arms supporting the hohlraum halves using a $150 \mu\text{m}$ thick, 2 mm diameter CH ablator. The line fit to the data gives a mode 1 sensitivity of $193 \mu\text{m/K}$.

Figure 4 shows the D-T layer mode 2 amplitude as the heater power on the each of the body heater is adjusted. The shim power is the calculated based on the current supplied to the hohlraum heaters and using the 40Ω resistance of the segment of the heater wound on the hohlraum body. The mode 2 sensitivity to power is $0.67 \mu\text{m/mW}$. Controlling the mode 2 to within $\pm 0.25 \mu\text{m}$, about half of the NIF requirement, requires controlling the power to within 0.37 mW which corresponds to 0.3 mA in current. As with mode 1, this requirement is readily achievable with current electronics.

In targets with beryllium capsules, control of these two modes has been shown to be sufficient to meet the low mode requirements for ignition shots. In CH targets, coupling of the shimming currents to non-axially symmetric modes results in low mode power slightly above specifications. This is due, in part, to the non-ideal construction of the hohlraum and target assembly and the resulting asymmetric heat conduction. Work is in progress to improve the axial symmetry of the targets to correct this.

Grain-boundary grooves

We have previously reported that the roughness in D-T fuel layers is due to localized low-angle grain-boundary grooves[20]. These grooves form as a result of defects in the solid during growth of the otherwise single-crystal. We have observed the groove profiles using the PSDI and find that the shape most often fits a Lorentzian, with the deviation from a

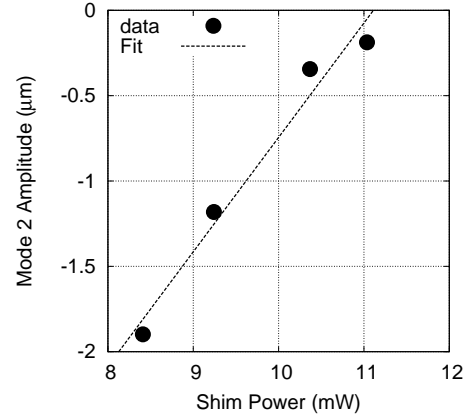


FIG. 4: Dependence of mode 2 amplitude of a $65 \mu\text{m}$ thick D-T layer on the power supplied to each of the hohlraum body heaters using a $150 \mu\text{m}$ thick, 2 mm diameter CH ablator. The line fit to the data gives a mode 2 sensitivity of $0.67 \mu\text{m/mW}$

flat profile given by

$$y = \frac{-d}{1 + \left(\frac{x}{w}\right)^2}, \quad (2)$$

where d is the depth of the groove and w is the half-width at half-maximum. This form can be integrated to give the total groove cross-sectional area of $A = \pi dw$. Figure 5 shows an example of a groove profile as measured by the PSDI (solid line) on a layer at $T_m - 0.15 \text{ K}$ and the corresponding fit (dotted line). This groove has depth of $4.5 \mu\text{m}$ and $w = 11.3 \mu\text{m}$, giving a cross-sectional area of $160 \mu\text{m}^2$.

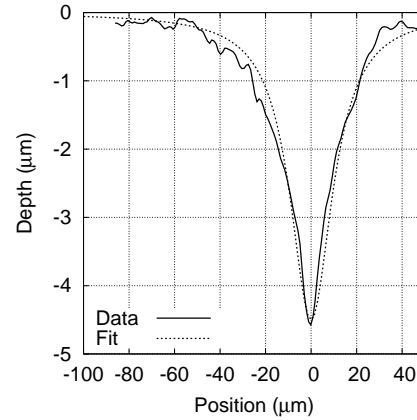


FIG. 5: Groove profile measured by the PSDI for a layer at $T_m - 0.15 \text{ K}$. The fit parameters, given by Eq. 2 are $d = 4.5 \mu\text{m}$ and $w = 11.3 \mu\text{m}$. The cross-sectional area is $160 \mu\text{m}^2$ and meets the requirement.

Figures 6 and 7 shows histograms of the groove depths and widths for those grooves measured by the PSDI. We find that the width tends to be relatively constant across the group, with a typical w of $15 \mu\text{m}$. The widths are also independent of the seeding method, having mean values of $15.7 \mu\text{m}$ and $14.5 \mu\text{m}$ for the good seeded and all layers, respectively. Therefore, to

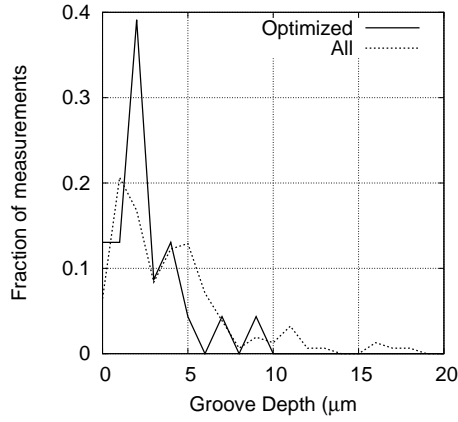


FIG. 6: Distribution of groove depths measured by the PSDI for both the optimized seeding method and all layering seedings.

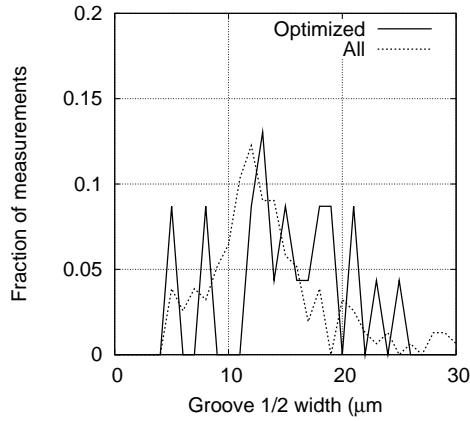


FIG. 7: Distribution of groove 1/2 widths (w) measured by the PSDI for both the optimized seeding and all layering seedings.

remain below A of $200 \mu\text{m}^2$ requires that the groove depths be less than $5 \mu\text{m}$. In contrast, the depths do differ between the seeding methods. Those seeded properly have fewer very deep grooves than the general population. The mean depth for properly seeded layers is $2.6 \mu\text{m}$, while that of all seeds is $4.1 \mu\text{m}$. The long tail in the distribution of depths for all layers is what drives the larger average depth. Figure 8 shows the cumulative probability for a groove area to be less than a given value. Again, we see that the good seeding method produces slightly more grooves that meet the cross-sectional area specification of $200 \mu\text{m}^2$ than all seeds, but that difference does not argue strongly that seeding is important.

The major difference between the two seeding methods is the number of grooves on a given layer. Figure 9 shows the number of grooves detected in the PSDI patch for both the optimized seeding protocol and the entire population. Here we see that a large fraction of the patches sampled have no detectable grooves when properly seeded, while the uncontrolled seeding population can have many grooves. Using Fig. 8 as a guide, 80% of the grooves meet the $200 \mu\text{m}^2$ cross-

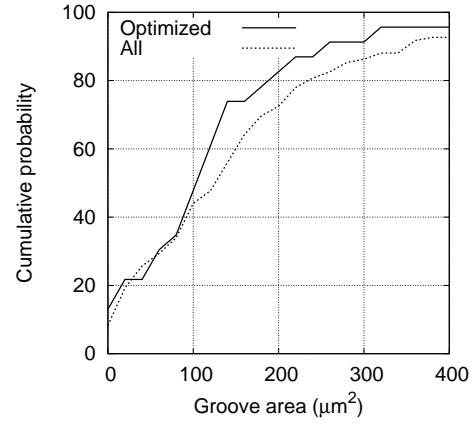


FIG. 8: Cumulative probability distribution of groove cross-section areas as measured by the PSDI for layers seeding using the optimized protocol and all layer seedings. The probability is that a given groove has area less than or equal to the specified value. Both seeding methods produce nearly 80% of grooves with areas less than $200 \mu\text{m}^2$, with the optimized seeding methods slightly better.

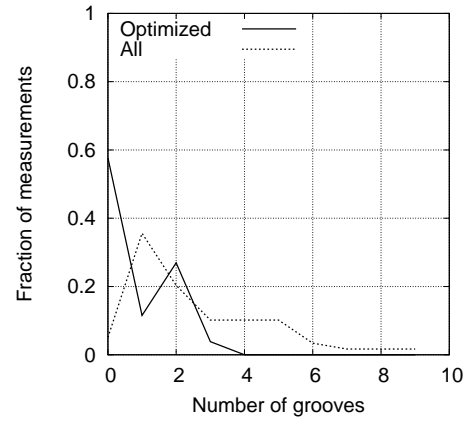


FIG. 9: Histogram of the number of grooves detected in the PSDI patch for the good seeding method and all seeds. The good seeding method produces far fewer grooves in the PSDI patch than the general seeding method. The sample size is 26 patches for the good seeding method and 53 patches for all seeding methods.

sectional area requirement. Thus a layer with 3 grooves has an approximately 50% chance of meeting the cross-sectional area requirement.

Characterization at NIF

The optical microscopy and interferometry characterization will not be available at the NIF. Instead, three orthogonal x-ray images will provide the characterization. Two of the views, through slots in the side of the hohlraum, will provide only a view of the D-T solid-vapor interface at the mid-plane of the capsule along their respective imaging directions. The third view, through the laser entrance hole (LEH), is unobstructed.

These three views do not enable full characterization of the D-T surface, particularly since the roughness tends to be localized at grooves. The grooves present several challenges. We have developed a characterization strategy that uses simulations and actual data to determine the fraction of layers that may have groove which exceed the specification but are not detected.

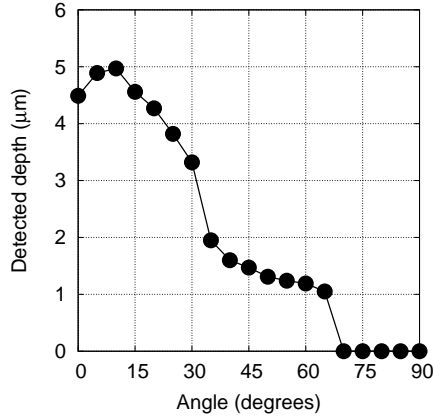


FIG. 10: Detected groove depth dependence on the angle between the groove and the x-ray imaging axis. The x-ray image was simulated using a groove $d = 6 \mu\text{m}$, $w = 15 \mu\text{m}$. Zero degrees corresponds to the groove length parallel to the imaging direction.

We have implemented a simple algorithm that detects grooves in the limb of the x-ray image. The algorithm searches for clusters of points that deviate from the local mean D-T layer position. This code was benchmarked using simulated radiographs. First, the ability to detect a groove depends on its orientation relative to the imaging direction. Grooves oriented along the imaging direction are easier to detect than those perpendicular to it. Simulated x-ray images were generated with the groove angle relative to the imaging direction varied from 0 (parallel to the imaging direction) up to 90 degrees. These images were then processed using the groove detection algorithm and compared to the input. Figure 10 shows the result for a case where a single groove with depth of $6 \mu\text{m}$ is placed in the simulated layer. First, the detected groove depth is always less than the $6 \mu\text{m}$ of the simulation, probably due to the finite pixel size. Grooves larger than 60° are not detected, with those between about 45° and 60° differing significantly from the groove depth in the simulated image. Additional simulations indicate that grooves need to have about $200 \mu\text{m}$ of length within the mid-plane of the capsule to be detected.

Using the above results it is possible to calculate the probability that a groove of a given length can be detected in any of the three x-ray views. The criteria for detection is that the groove needs to have a length of at least $200 \mu\text{m}$ within the mid-plane of a given imaging direction and that it is oriented less than 45° to the imaging direction. Figure 11 shows the result of a Monte-Carlo style model where a groove of a specified length is placed on the sphere at random positions and

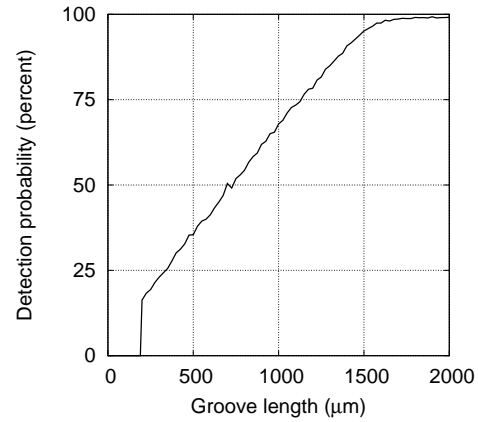


FIG. 11: Probability to detect a groove with specified length in any of the three x-ray views available for NIF. This is calculated by placing a groove with random position and orientation and determining if it meets the detection criteria in any of the three views.

angles. The groove is checked to see if it meets the detection criteria in any of the three views. The figure shows that the grooves need to be about $2000 \mu\text{m}$ long (about $1/3$ the capsule circumference) to be detected with near certainty. Unfortunately, significantly shorter grooves are often observed and their probability of detection can be quite low.

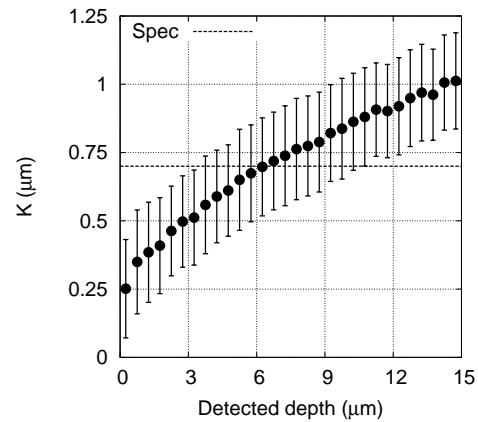


FIG. 12: Calculated probability of K for a layer given a measured total groove depth. The circle indicates the mean K for a specific measured depth and the error bars represent the standard deviation. The required K of $0.7 \mu\text{m}$ is indicated by the dashed line.

Finally, we can combine the simulation results above with grooves observed by the PSDI on D-T layers to develop a metric that gives the probability that a given layer meets the requirements. The procedure is to take a real groove depth, width, and length and randomly place it on the spherical surface in the simulation. The groove's actual contribution to K and the detected depth in the simulation are calculated for many positions on the spherical surface. We histogram the resulting K values for a given detected depth, calculating the mean and standard deviation in K for a given detected depth.

Figure 12 shows the result using a population of 23 groove measurements. The mean value of K reaches the $K = 0.7 \mu\text{m}$ specification for a total measured groove depth of about $6 \mu\text{m}$. This is the level where the layer has a 50% chance of passing the specification. The probability the layer meets the K requirement is 70% at 3μ of total detected depth. In practice this means that no more than one groove can be detected in all three NIF x-ray views for the layer to meet the K requirement. Unfortunately, the same method cannot be applied to the maximum groove area since one groove with $A > 200 \mu\text{m}^2$ is enough to cause the layer to fail and the groove length and orientation can be such that it is often missed in the three x-ray views.

RAPID COOLING

The observation that the roughness at 19.6 K is half that at 18.3 K following a slow-cool protocol motivated us to study rapidly cooling the layers to 18.3 K. This is also partly motivated by early work with D_2 layers [6, 23, 24]. The short time scales motivated us to observe the layers with visible light rather than x-rays during the rapid-cooling to capture the dynamics. Thus, rapid-cooling results are primarily limited to the plastic capsule.

D-T layers were formed as for the slow-cooling studies, but cooling was paused at 19.5 - 19.65 K. The layer was then cooled over 5 - 600 s to 18.3 K. The RMS roughness and optical image, when focused at the capsule midplane, show little change upon reaching 18.3 K, as previously described [15]. However, upon closer inspection using a higher resolution microscope over a smaller field of view, we found that localized defects began to appear at approximately 18.9 K.

We have characterized layers during rapid cooling using the interferometer to better characterize the roughness. Figure 13 shows a height-map of a layer at several stages during cooling. The first image (a) shows the layer just before cooling. A horizontal defect is located on the left side of the image, a faint curved structure runs mostly vertically through the center of the image, and a shallow defect is visible on the right side. The remaining structure is measurement noise due to mechanical vibrations. The second image (b) shows the layer just upon reaching $T_m - 1.2$ K. There is little change in the surface between images (a) and (b). The third image, (c), is taken just as the layer reaches $T_m - 1.5$ K. Faint lines, in a periodic circular pattern, are visible centered about the left and right sides of the image. The center of the circular pattern corresponds to the poles of the sphere with respect to the crystal growth direction. The pattern continues to get deeper with time, as shown in (d). Figure 14 shows the PSD obtained from the four images in Fig. 13. The structure at $T_m - 1.5$ K + 8 s is just below the D-T PSD requirement for modes 80 - 160. Thus we conclude that the rapid cooling will be successful assuming that the NIF shot is taken within a few seconds of reaching $T_m - 1.5$ K.

The roughness at a given temperature during rapid cool-

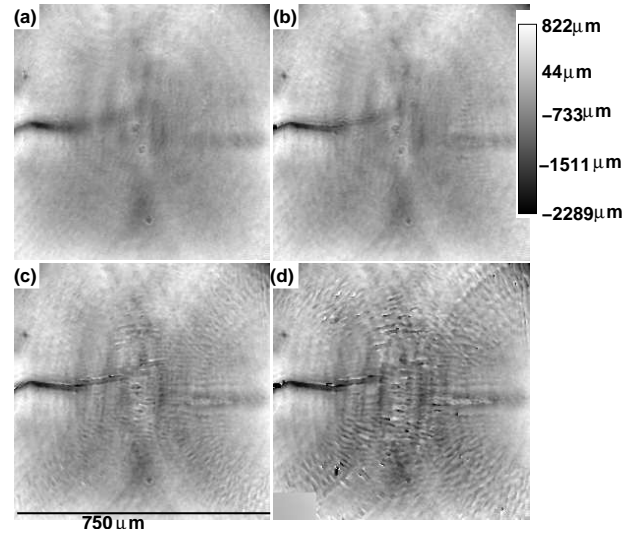


FIG. 13: Height maps from the PSDI obtained during a rapid cool of a D-T layer showing the evolving structure with time. Panel (a) is taken before the cooling begins. One groove is visible on the left side of the image. Panel (b) is taken when the layer has reached $T_m - 1.2$ K and shows little change in the structure from (a). (c) is taken when the layer reaches $T_m - 1.5$ K and shows the evolution of small grooves. Note the circular patterns centered to the left and right sides of the image which are associated with the poles of the crystal axes. (d) is taken 8 s after reaching $T_m - 1.5$ K and show the continued evolution of defects.

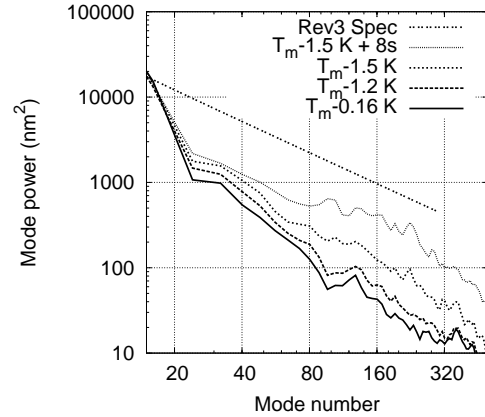


FIG. 14: Power spectral distribution (PSD) plots as measured with the PSDI during rapid-cooling of the layer. The cooling was over 30 s to 1.5 K below the melting temperature (T_m). The layer starts well below the D-T surface roughness requirement at $T_m - 0.16$ K. The roughness begins to noticeably increase upon reaching $T_m - 1.2$ K, but is still well below the requirement upon reaching $T_m - 1.5$ K. The roughness is nearly to the requirement after 8 s at $T_m - 1.5$ K for modes 100-200.

ing also depends on the cooling rate. Cooling slowly allows the defects to aggregate and the layer to roughen with time. We find what appear to be two distinct classes of defects, corresponding roughly to lines of latitude and longitude, with respect to the crystal c-axis. The lines of latitude

Neon doped D₂

typically remain small, but appear at nearly the same temperature regardless of cooling rate. These are a result of slip along basal planes[21]. The second class of defects, along lines of longitude, appear later in time and aggregate into a 6-fold symmetry pattern and are a result of grain-boundary polygonization[21]. Figure 15 shows the temperature where each defect is first observed as a function of cooling rate. The slip defects appear by $T_m - 1$ K, regardless of cooling rate, whereas the polygonization does depend on the cooling rate. Slip depends only on the applied stress, which is a function of the temperature but not the rate. The polygonization process relies on agglomeration of defects which takes some time and hence is dependent on the cooling rate.

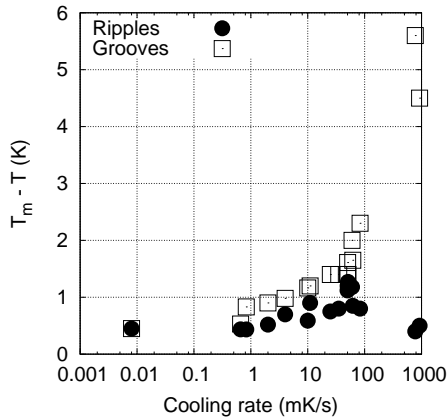


FIG. 15: Temperature when the appearance of the slip (circles) and polygonization (squares) defects appear on the D-T surface as a function of the cooling rate. The slip process is insensitive to the cooling rate as it depends only on the thermal stress.

One concern with the rapid cooling approach is that the larger thermal contraction of the D-T compared to the shell will result in the D-T layer detaching from the shell. The resulting density perturbation would have a negative effect on ignition. We have several pieces of evidence that the D-T does not detach from the shell. First, we observe a contraction of the plastic shell during cooling that is consistent with the stress induced by the D-T layer. Second, this contraction is asymmetric in D-T layers that are single-crystal. Specifically, the contraction along the c-axis is much larger than along the a-axis. The plastic capsule becomes slightly ellipsoidal. Finally, we have observed a sudden detachment of the D-T layer from the shell wall when the layer is cooled at rates of 0.5 - 1.0 K/s to less than 14 K. This detachment is typically at one or two regions of the capsule and localized to a few hundred microns. We observe the capsule to contract with the D-T layer up until the point when the D-T attachment fails. These points provide confidence that the fuel layer remains in contact with the shell under typical cooling of ≈ 1.5 K on time scales of tens of seconds.

In a series of separate experiments, we studied the growth and rapid cooling of D₂ fuel layers and layers with small amounts of Ne (0.4%) added to D₂. We simulate the volumetric heat generation from tritium radioactive decay in D-T by placing the capsule in an integrating sphere and illuminating the sphere with with 3.16 μm infrared (IR) laser. The integrating sphere produces a more uniform IR distribution on the capsule. The amount of IR absorption by the D₂ corresponds to about 1.2 to 1.5 times the beta-decay volumetric heating.

We have observed many similarities between the D₂ and the D-T layers including the "arctic circle" features, layers that show c-axis growth from what appears to be a fill-tube initiation, and the slip bands and grooves oriented with the c-axis after rapid cooling. There are two results that are worth mentioning here. First, the motivation for adding a small amount of Ne is that we speculated that the presence of Ne would allow the D₂ solid to adapt to the stress induced by thermal contraction during rapid cooling by inhibiting slip and grain boundary polygonization. We added 0.4% Ne to the D₂ gas by mixing at fixed volume and temperature a known amount of pressure of each gas. The shell was then filled with this gas mixture. This amount of Ne was small enough to keep remain soluble in the solid D₂. This understanding was obtained from the most recent phase diagrams for D₂ and Ne[25]. The resulting solid layers contained significantly more roughness than the D₂ layers and tended to grow much more non uniformly. If the Ne was removed from the D₂ then we were once again able to grow low roughness ice layers. Nevertheless, we continued to explore the effect of rapid cool on the Ne-doped D₂ layers and found that they too exhibited arctic circles as well as grain-boundary grooves. We were unable to form an initial Ne-doped D₂ layers with no sign of roughness so it is not clear whether this would have led to layers with greater capacity to withstand the stress due to rapid cooling.

The second result for the Ne-doped D₂ layers is that we investigated the effect of temperature oscillations. This has been studied in D-T and the results are confusing. In these experiments the ice layer undergoes rapid cooling to about 1.5 K below the melting temperature. Then, after the roughness has stopped evolving, the temperature of the system is varied either with a step function or with a sinusoidal variation with an amplitude ranging from 0.1 K to up to 1.3 K with a time period which is long compared to the thermal time constant of the system but short compared to the layering time. We found that the Ne-doped D₂ layers did not show improvement with temperature oscillations for a wide matrix of oscillation amplitudes and time-periods. The defects which appeared during the rapid cool seem to be imprinted on the layer and temperature oscillations appeared to lessen the visibility of these features during the increase in temperature but they always reappeared on cool down. Although these experiments never started with a highly smooth ice layer we believe there is sufficient evidence to conclude that the addition of Ne to the

D₂ did not improve the quality of layers or make them robust to shrink-stress induced cracks and ripples. We expect that a similar result would be observed with Ne-doped D-T layers.

SUMMARY

High quality fuel layers that meet the NIF ignition requirements remain a challenge to reliably produce. We have demonstrated that thermal shimming of targets can meet the low mode requirements, with work remaining on target construction to improve the non-axial components. Similarly, formation of a single D-T crystal greatly reduces the number of grain-boundary grooves, and high local defects, in the fuel layer. Our recent experience has provided a method to produce single crystal layer with only the three x-rays views at the NIF target chamber. The experience with plastic capsules using backlit microscopy and interferometry allows us to estimate the probability of missing grooves with the three x-ray views. Finally, once the layer has been formed and characterized, rapidly cooling over tens of seconds preserves the layer quality for approximately 5 s, which provides enough time for the laser shot.

This work performed under the auspices of the U.S. Department of Energy by Lawrence Livermore National Laboratory under Contract DE-AC52-07NA27344.

-
- [1] S. W. Haan and ..., Fusion Science and Technology **This issue** (2010).
 - [2] J. K. Hoffer and L. R. Foreman, Phys. Rev. Lett. **60**, 1310 (1988).
 - [3] A. J. Martin, R. J. Simms, and R. B. Jacobs, J. Vac. Sci. Technol. A **6**, 1885 (1988).
 - [4] D. R. Harding, D. D. Meyerhofer, S. J. Loucks, L. D. Lund, R. Janezic, L. M. Elasky, T. H. Hinterman, D. H. Edgell, W. Seka, M. D. Wittman, et al., Physics of Plasmas **13**, 056316 (2006).
 - [5] T. C. Sangster, R. Betti, R. S. Craxton, J. A. Delettrez, D. H. Edgell, L. M. Elasky, V. Y. Glebov, V. N. Goncharov, D. R. Harding, D. Jacobs-Perkins, et al., PHYSICS OF PLASMAS **14** (2007).
 - [6] M. Martin, C. Gauvin, A. Choux, P. Baclet, and G. Pascal, Fusion Science and Technology **49**, 600 (2006).
 - [7] J. Moody, B. Kozioziemski, E. Mapoles, J. Sater, E. Dewald, J. Koch, N. Izumi, A. Chernov, J. Salmonson, R. Montesanti, et al., in *Journal of Physics: Conference Series* (IOP Publishing Ltd., UK, 2008), p. 032064.
 - [8] P. S. Ebey, J. M. Dole, D. A. Geller, J. K. Hoffer, J. Morris, A. Nobile, J. R. Schoonover, D. Wilson, M. Bonino, D. Harding, et al., FUSION SCIENCE AND TECHNOLOGY **54**, 375 (2008).
 - [9] E. Koresheva, I. Osipov, T. Timasheva, and L. Yaguzinskiy, Journal of Physics D: Applied Physics pp. 825–830 (2002).
 - [10] D. N. Bittner, G. W. Collins, E. Monsler, and S. Letts, Fusion Technology **35**, 244 (1999).
 - [11] B. J. Kozioziemski, R. L. McEachern, R. A. London, and D. N. Bittner, Fusion Science and Technology **41**, 296 (2002).
 - [12] R. C. Cook, M. Anthamatten, and S. A. Letts, Fusion Science and Technology **45**, 148 (2004).
 - [13] J. J. Sanchez and W. H. Giedt, Fusion Tech. **36**, 346 (2000).
 - [14] J. D. Moody, B. J. Kozioziemski, R. L. London, D. S. Montgomery, J. J. Sanchez, J. D. Sater, D. N. Bittner, J. A. Burmann, R. L. Jones, J. Pipes, et al., Journal De Physique IV **133**, 863 (2006).
 - [15] R. C. Cook, B. J. Kozioziemski, A. Nikroo, H. L. Wilkens, S. Bhandarkar, A. C. Forsman, S. W. Haan, M. L. Hoppe, H. Huang, E. Mapoles, et al., Laser and Particle Beams **26**, 479 (2008).
 - [16] J. A. Koch, T. P. Bernat, G. W. Collins, B. A. Hammel, B. J. Kozioziemski, A. J. MacKinnon, J. D. Sater, D. N. Bittner, and Y. Lee, Fusion Technology **38**, 123 (2000).
 - [17] B. J. Kozioziemski, J. D. Sater, J. D. Moody, J. J. Sanchez, R. A. London, A. Barty, H. E. Martz, and D. S. Montgomery, Journal of Applied Physics **98**, 103105 (2005).
 - [18] D. S. Montgomery, A. Nobile, and P. J. Walsh, Review of Scientific Instruments **75**, 3986 (2004).
 - [19] P. C. Souers, *Hydrogen Properties for Fusion Energy* (University of California, Berkeley, 1986).
 - [20] A. A. Chernov, B. J. Kozioziemski, J. A. Koch, L. J. Atherton, M. A. Johnson, A. V. Hamza, S. O. Kucheyev, J. B. Lugten, E. A. Mapoles, J. D. Moody, et al., Applied Physics Letters **94**, 064105 (pages 3) (2009).
 - [21] B. J. Kozioziemski, S. O. Kucheyev, J. B. Lugten, J. A. Koch, J. D. Moody, A. A. Chernov, E. A. Mapoles, A. V. Hamza, and L. J. Atherton, Journal of Applied Physics **105**, 093512 (pages 5) (2009), URL <http://link.aip.org/link/?JAP/105/093512/1>.
 - [22] B. J. Kozioziemski, A. A. Chernov, E. R. Mapoles, and J. D. Sater, Submitted to Physical Review Letters (2010).
 - [23] D. Bittner (13th Target Fabrication Specialists Meeting, Catalina Island, CA, 1999).
 - [24] M. Martin, C. Gauvin, A. Choux, P. Baclet, and G. Pascal, Fusion Science and Technology **51**, 747 (2007).
 - [25] V. G. Belan, N. N. Gal'tsov, A. I. PRokhvatilov, and M. A. Strzhemechnyi, Low Temperature Physics **31**, 947 (2005).